# Nanosecond Pulsed Plasma Activated C2H4/O2/Ar Mixtures in a Flow Reactor

Suo Yang,* Xiang Gao,* Vigor Yang,† and Wenting Sun‡
*Georgia Institute of Technology, Atlanta, Georgia 30332*
Sharath Nagaraja§
*General Electric Global Research, Schenectady, New York 12301*
and
Joseph K. Lefkowitz¶ and Yiguang Ju**
*Princeton University, Princeton, New Jersey 08544*

The present work combines numerical and experimental efforts to investigate the effect of nanosecond pulsed plasma discharges on the low-temperature oxidation of $C_2H_4/O_2/Ar$ mixtures under reduced pressure conditions. The nonequilibrium plasma discharge is modeled using a one-dimensional framework, employing separate electron and neutral gas temperatures, and using a detailed plasma and combustion chemical kinetic mechanism. Good agreement is seen between the numerical and experimental results, and both results show that plasma enables low-temperature $C_2H_4$ oxidation. Compared to zero-dimensional modeling, the one-dimensional modeling significantly improves predictions, probably because it produces a more complete physical description (including sheath formation and accurate reduced electric field). Furthermore, the one- and zero-dimensional models show very different reaction pathways, using the same chemical kinetic mechanism and thus suggest different interpretations of the experimental results. Two kinetic mechanisms (HP-Mech and USC Mech-II) are examined in this study. The modeling results from HP-Mech agree better with the experimental results than those of USC Mech-II because USC Mech-II does not include the $OH + C_2H_4 = CH_2CH_2OH$ reaction pathway. The model shows that 75–77% of the input pulse energy is consumed during the breakdown process in electron impact dissociation, excitation, and ionization reactions, which efficiently produce reactive radical species, fuel fragments, and excited species. The modeling results using HP-Mech reveal that reactions between $O(^1D)$ and $C_2H_4$ generate 24% of OH, 19% of HCO, 60% of $CH_3$, 63% of $CH_2$, and 17% of $CH_2O$. These in turn significantly enhance hydrocarbon oxidation, since 83% of CO comes from HCO and 53% of $CO_2$ comes from $CH_2$ under the present low-temperature environment and short time scale.

## Nomenclature

| | | |
|---|---|---|
| $E$ | = | electric field, $V \cdot cm^{-1}$ |
| $F_i^{EHD}$ | = | electrohydrodynamic force per unit volume, $kg \cdot cm^{-2} \cdot s^{-1}$ |
| $G(t)$ | = | nondimensional heat transfer parameter |
| $J_{e,s}$ | = | wall boundary flux of electrons, $cm^{-2} \cdot s^{-1}$ |
| $J_k$ | = | flux of $k$th species, $cm^{-2} \cdot s^{-1}$ |
| $J_\epsilon$ | = | flux of electron energy, $eV \cdot cm^{-2} \cdot s^{-1}$ |
| $J_{\epsilon,s}$ | = | wall boundary flux of electron energy, $eV \cdot cm^{-2} \cdot s^{-1}$ |
| $J_{+,s}$ | = | wall boundary flux of positive ions, $cm^{-2} \cdot s^{-1}$ |
| $J_{-,s}$ | = | wall boundary flux of negative ions, $cm^{-2} \cdot s^{-1}$ |
| $J_{+,-}$ | = | net positive and negative charge fluxes, respectively, $cm^{-2} \cdot s^{-1}$ |
| $k_d$ | = | thermal conductivity of quartz, $W \cdot m^{-1} \cdot K^{-1}$ |
| $k_{gw}$ | = | thermal conductivity of gas mixture at temperature $T_{gw}$, $W \cdot m^{-1} \cdot K^{-1}$ |
| $L$ | = | gap length, cm |
| $l_d$ | = | thickness of dielectric layer, cm |
| $n_e$ | = | electron density, $cm^{-3}$ |
| $n_k$ | = | number density of $k$th species, $cm^{-3}$ |
| $\boldsymbol{n}_s$ | = | outward unit normal vector |
| $n_\epsilon$ | = | electron energy density, $eV \cdot cm^{-3}$ |
| $n_{+,-}$ | = | sum of number densities of positive and negative ions, respectively, $cm^{-3}$ |
| $p$ | = | pressure, $kg \cdot cm^{-1} \cdot s^{-1}$ |
| $\dot{Q}_\epsilon$ | = | production rate of electron energy density, $eV \cdot cm^{-3} \cdot s^{-1}$ |
| $\dot{Q}^{JH}$ | = | energy release rate from Joule heating, $kg \cdot cm^{-1} \cdot s^{-3}$ |
| $q_i$ | = | energy flux from heat conduction and diffusion, $kg \cdot s^{-3}$ |
| $T$ | = | temperature, K |
| $T_{amb}$ | = | ambient temperature, K |
| $T_b$ | = | boundary temperature, K |
| $T_{gw}$ | = | gas temperature at a distance $\Delta x$ from solid wall, K |
| $T_{se}$ | = | temperature of secondary electrons ejected from electrode surface, eV |
| $u_i, u_j$ | = | flow velocity components in $i$th and $j$th directions, respectively, $cm \cdot s^{-1}$ |
| $V_{app}$ | = | applied voltage, V |
| $V_{gap}$ | = | gap voltage, V |
| $\gamma$ | = | secondary electron emission coefficient for ions colliding with electrode surface |
| $\epsilon$ | = | electric permittivity, $F \cdot cm^{-1}$ |
| $\epsilon_d$ | = | dielectric constant |
| $\epsilon_e$ | = | electron energy, eV |
| $\rho$ | = | density of plasma mixture, $kg \cdot cm^{-3}$ |
| $\tau_{ij}$ | = | viscous shear stress tensor, $kg \cdot cm^{-1} \cdot s^{-2}$ |

*Graduate Student, School of Aerospace Engineering. Student Member AIAA.
†William R. T. Oakes Professor and Chair, School of Aerospace Engineering. Fellow AIAA.
‡Assistant Professor, School of Aerospace Engineering. Member AIAA.
§Research Engineer, Combustion Dynamics Laboratory. Member AIAA.
¶Graduate Student, Department of Mechanical and Aerospace Engineering. Student Member AIAA.
**Robert Porter Patterson Professor, Department of Mechanical and Aerospace Engineering. Associate Fellow AIAA.

$\phi$    =    electric potential, V
$\dot{\omega}_k$    =    production term of $k$th species, $cm^{-3} \cdot s^{-1}$

## I.   Introduction

OVER the past few years, nonequilibrium plasma discharges have shown great potential to enhance and stabilize the combustion process in internal combustion engines, gas turbines, and scramjet engines [1–4]. Experiments have demonstrated that plasmas can shorten ignition delay times [5–11], extend extinction limits [12,13], improve flame stabilization [12,14], increase flame speed [6,15], and suppress soot formation [15,16]. Unfortunately, most of the studies mentioned focus on the phenomenological impacts of plasma assisted combustion (PAC), and the underlying physical and chemical mechanisms of plasma enhancement remain less understood. In particular, it is still unclear which reaction pathways are dominant and which reaction pathways may be missing. To answer this question, a combination of experimental and numerical efforts is required. Significant progress has been made in investigating the underlying kinetic mechanisms of plasma assisted combustion. For example, Sun et al. [17] integrated an *in situ* nanosecond discharge with a counterflow burner to study the plasma effects on a $CH_4$-air diffusion flame. The *in situ* pulsed plasma discharge was found to modify $CH_4$ oxidation pathways through atomic oxygen production. A new ignition/extinction curve without hysteresis was achieved and resulted in improved flame stabilization and a dramatic extension of the extinction limits.

The mechanism of plasma/combustion interaction is still, however, not well understood, due to the complicated thermal, kinetic, and transport coupling between plasma and combustion kinetics typical of the experimental platforms used in PAC studies. For example, the fuel jet in the crossflow studied by Kim et al. [18], the supersonic reacting flow studied by Starikovskaia [10] and Leonov et al. [11,19], and the swirling reacting flow studied by Moeck et al. [14] have complex flow structures even without plasma. It is extremely difficult to isolate and understand the underlying kinetics responsible for plasma enhancement in such highly coupled configurations. For this reason, a few configurations have been designed to simplify or eliminate the hydrodynamic effects so that PAC kinetic enhancement can be isolated from other effects.

Uddi et al. [20] conducted two photon absorption laser-induced fluorescence measurements of atomic oxygen for air/fuel nanosecond pulsed discharges in a rectangular quartz flow reactor. The peak mole fraction of atomic oxygen in a stoichiometric methane/air mixture was found to be approximately equal to that in pure air, but the rate of decay was found to be faster due to fuel oxidation. Discharge kinetic modeling calculations provided good overall agreement with all of the experimental data and suggested key processes of atomic oxygen generation and decay.

Yin et al. [21] studied the ignition of mildly preheated (100–200° C) $H_2$/air mixtures subjected to nanosecond pulsed discharges in a quartz reactor. The number of pulses leading to ignition was found to be inversely proportional to pressure but a weak function of the mixture equivalence ratio. It was also found that the number of pulses required for ignition was nonlinearly dependent on the pulsing frequency. At a given temperature and pressure, there existed an optimum repetition rate at which the number of pulses needed for ignition reached a minimum. In the same plasma flow reactor setup, Yin et al. [22] conducted OH density measurements in a decaying plasma after a burst of nanosecond pulses in $H_2$/air, $CH_4$/air, $C_2H_4$/air, and $C_3H_8$/air mixtures. It was observed that OH densities are nearly independent of the equivalence ratio in the $H_2$/air mixture but higher under lean conditions in $CH_4$/air, $C_2H_4$/air, and $C_3H_8$/air mixtures. Similar studies were conducted by Mintusov et al. [23] for ethylene $(C_2H_4)$/air flows in the same reactor. Lefkowitz et al. [24,25] conducted *in situ* measurements of nanosecond pulsed plasma-activated $C_2H_4$/Ar pyrolysis and oxidation of $C_2H_4/O_2$/Ar mixtures in a low-temperature flow reactor. Midinfrared laser absorption spectroscopy was used to measure $C_2H_2$, $CH_4$, and $H_2O$ densities and was cross validated with micro-gas-chromatography sampling. Simulations using a zero-

dimensional (0D) kinetic model were conducted using USC Mech-II [26] and HP-Mech [27,28] chemical reaction models to gain further insight into the plasma activation process. Path flux analysis of methane oxidation suggested that plasma-generated radicals create a low-temperature oxidation pathway via $RO_2$ chemistry, which is responsible for the formation of oxygenated species. Large discrepancies were observed between the measured and predicted $H_2O$ and $CH_4$ densities, suggesting large uncertainties in either the physical model or the kinetic model or both. In addition, ambiguities in the criteria for choosing the values of reduced electric field (E/N) and electron density also introduced significant uncertainties to the 0D modeling.

Although there have been a number of experimental studies, there have been only a few detailed numerical studies of PAC. Numerical simulation can be immensely helpful, in that it complements experimental efforts and can provide significant insights into plasma enhancement of the combustion process. The multiscale nature of PAC, however, creates enormous challenges for conducting comprehensive modeling studies. Consequently, several studies have resorted to simplified 0D kinetic models in order to begin to illuminate the plasma kinetic and thermal effects in fuel/air mixtures [21,22,24,25,29]. In these simulations, the plasma discharge was assumed to be uniform over the entire domain during each voltage pulse. The reduced electric field and electron density values were prespecified such that the coupled energy matched that of the experiments. Modeling energy input channels for the plasma discharge created difficulties, however, in the 0D models. The model did not consider sheath formation, which has a significant influence on plasma properties. In addition, mass and thermal diffusion effects were ignored.

Recently, Nagaraja et al. [7,30,31] and Yang et al. [6,32] developed a self-consistent, one-dimensional (1D) numerical framework to simulate pulsed nanosecond discharges in fuel/air mixtures. The model is capable of resolving the transient electric field during each nanosecond discharge pulse as well as calculating the cumulative effects of multiple pulses on fuel oxidation and combustion. The model has been extensively validated with input energy, atomic oxygen density, and gas temperature measurements of nanosecond pulsed air discharges in plane-to-plane geometry [31]. The modeling results also showed good agreement with OH density and ignition delay measurements in $H_2$/air mixtures subjected to pulsed, nanosecond discharges in a plasma flow reactor [7].

Despite the previously mentioned efforts, the effect of low-temperature plasma on the ignition of hydrocarbon fuel/air mixtures still presents significant uncertainties. There is a need to investigate the plasma/combustion interaction mechanisms for hydrocarbon fuels using advanced optical measurements and self-consistent numerical simulations.

The present work combines experimental and numerical efforts to investigate the effect of low-temperature, nonequilibrium plasma discharges on the oxidation of $C_2H_4/O_2$/Ar mixtures. A time-accurate 1D model [7,31] is used to simulate the species and temperature evolution across the discharge gap, and the results are compared with the mid-IR speciation measurements in plasma-activated ethylene oxidation reported by Lefkowitz et al. [25]. Detailed analysis is conducted to understand the various kinetic pathways through which the plasma-generated reactive species affect the hydrocarbon fuel oxidation process.

## II.   Experimental Setup

A detailed discussion of the experimental platform can be found in [25], and it is only briefly described here. The experiment was conducted in a rectangular $152 \times 45 \times 14$ $mm^3$ quartz and Macor flow reactor. Figure 1a shows a schematic of the reactor. The stainless steel electrodes $(2 \times 45 \times 45$ $mm^3)$ are housed in the top and bottom walls of the quartz section with a 1.6 mm dielectric barrier thickness, along with a silicone rubber sheet of 0.8 mm thickness to prevent air discharge on the surface of the electrodes. Plane-to-plane dielectric barrier discharges were used to generate homogeneous plasma, which justified the use of the 1D model. The applied high-voltage pulse was 8.83 ns at full width at half maximum and 9.23 kV at the
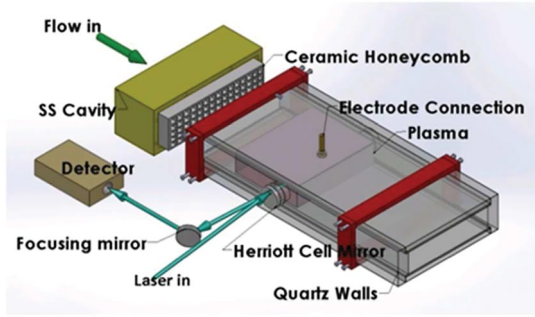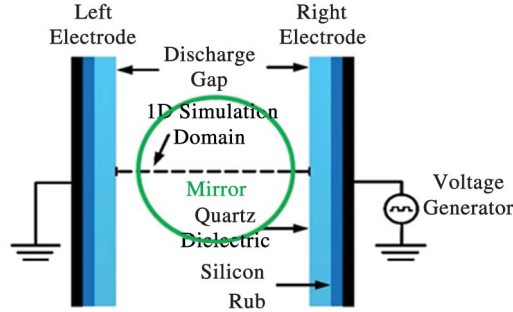
**Fig. 1 a) Schematic of the plane-to-plane plasma reactor [25]. b) Geometry of the simulation model.**

peak with a 30 kHz repetition frequency. Each experiment was conducted using a burst of 150 pulses. Experiments were conducted at a flow velocity of 0.4 m/s, pressure of 60 torr, and an initial temperature of 300 K. These low flow velocities allowed isolation of the chemical and thermal coupling from convective transport processes, offering better access to the underlying kinetic pathways, and also assured a long lifetime of the gas molecules in the plasma region relative to the duration of the plasma discharge.

Measurements of species and gas temperature were conducted using tunable diode laser spectroscopy. An external cavity mode hop free quantum cascade laser (Daulight Solutions) was coupled into a 24 pass miniature Herriott cell for a total path length of 1.08 m through the plasma region. The absorption lines used for $H_2O$ and temperature quantification were located at 1338.55 and 1339.15 $cm^{-1}$, the line for $C_2H_2$ quantification was at 1342.35 $cm^{-1}$, and the line for $CH_4$ quantification was at 1341.32 $cm^{-1}$. The uncertainties of the measurements of $C_2H_2$, $CH_4$, and gas temperatures were at most 10%, and that of $H_2O$ was at most 20%. The gas temperature was calculated by scanning over two different absorption lines of $H_2O$ at the same delay after the pulse burst.

## III.  Theoretical Framework

### A.  Simulation Configuration

The geometry of the numerical model is shown in Fig. 1b. The numerical model considers a particular cross-section of the flow reactor, and the computational domain is 14 mm long from the left electrode to the right electrode. The voltage pulses are applied at the right electrode, and the left electrode is connected to the ground.

### B.  Governing Equations, and Initial/Boundary Conditions

The model contains the Poisson equation for electric potential, the electron energy equation, and species continuity equations for all charged and neutral species given by Eqs. (1–3), respectively,

$$\nabla \cdot (\epsilon \nabla \phi) = -e(n_+ - n_- - n_e) \tag{1}$$

$$\frac{\partial n_\epsilon}{\partial t} + \nabla \cdot \boldsymbol{J}_\epsilon = \dot{Q}_\epsilon \tag{2}$$

$$\frac{\partial n_k}{\partial t} + \nabla \cdot \boldsymbol{J}_k = \dot{\omega}_k \tag{3}$$

where the electron energy density $n_\epsilon$ is given by the product of the electron density $n_e$ and electron energy $\epsilon_e$. The transport of energy and species is calculated by the drift (mobility-) diffusion model. The reduced electric field (E/N) and energy input can then be calculated rather than prespecified as in the 0D model [25].

The gas flow is modeled by solving the mass, momentum, and total energy conservation equations simultaneously, as given by Eqs. (4–6), respectively,

$$\frac{\partial \rho}{\partial t} + \frac{\partial \rho u_i}{\partial x_i} = 0 \tag{4}$$

$$\frac{\partial \rho u_i}{\partial t} + \frac{\partial (\rho u_i u_j)}{\partial x_j} = -\frac{\partial p}{\partial x_i} + \frac{\partial \tau_{ij}}{\partial x_j} + F_i^{\text{EHD}} \tag{5}$$

$$\frac{\partial \rho E}{\partial t} + \frac{\partial [(\rho E + p)u_i]}{\partial x_i} = -\frac{\partial q_i}{\partial x_i} + \frac{\partial (u_i \tau_{ij})}{\partial x_j} + \dot{Q}^{\text{JH}} \tag{6}$$

Unlike equilibrium plasma, which transfers electrical energy only into sensible enthalpy, Joule heating in nonequilibrium plasma transfers electrical energy into the total energy of the gas mixture. This means that not all energy from Joule heating contributes to a gas temperature rise. Heat release from chemical reactions is implicitly included in the unsteady term of the total energy, with the form of chemical energy converting to sensible enthalpy.

The simulations were conducted at pressure $p = 60$ torr, and initial temperature $T = 300$ K to match the experiments [25]. The initial mixture composition was $C_2H_4 : Ar : O_2 = 0.062 : 0.75 : 0.18$ in mole fractions.

The zero potential was set at the left boundary, and the gap voltage $V_{\text{gap}}$ was set at the right boundary. $V_{\text{gap}}$ is obtained from the applied voltage $V_{\text{app}}$ by using equation [33]

$$\frac{dV_{\text{app}}}{dt} = \left(1 + \frac{2l_d}{\epsilon_d L}\right)\frac{dV_{\text{gap}}}{dt} - \frac{2l_d e}{\epsilon_d \epsilon_0 L}\int_0^L [J_+ - J_-]\,dx \tag{7}$$

where the dielectric constant $\epsilon_d$ is 4.8 for quartz and 3.2 for silicone rubber.

A zero flux wall boundary condition is used for neutral species. The wall boundary fluxes for electrons, positive ions, negative ions, and electron energy are given by Eqs. (8–11), respectively [34],

$$\boldsymbol{J}_{e,s} \cdot \boldsymbol{n}_s = \frac{1}{4}n_e\sqrt{\frac{8k_b T_e}{\pi m_e}} + (a-1)\mu_e n_e \boldsymbol{E} \cdot \boldsymbol{n}_s - a\sum_k \gamma \boldsymbol{J}_{+k,s} \cdot \boldsymbol{n}_s \tag{8}$$

$$\boldsymbol{J}_{+,s} \cdot \boldsymbol{n}_s = \frac{1}{4}n_+\sqrt{\frac{8k_b T_g}{\pi m_+}} + a\mu_+ n_+ \boldsymbol{E} \cdot \boldsymbol{n}_s \tag{9}$$

$$\boldsymbol{J}_{-,s} \cdot \boldsymbol{n}_s = \frac{1}{4}n_-\sqrt{\frac{8k_b T_g}{\pi m_-}} + (a-1)\mu_- n_- \boldsymbol{E} \cdot \boldsymbol{n}_s \tag{10}$$

$$\boldsymbol{J}_{\epsilon,s} \cdot \boldsymbol{n}_s = \left(\frac{5}{2}k_b T_e\right)\left[\frac{1}{4}n_e\sqrt{\frac{8k_b T_e}{\pi m_e}} + (a-1)\mu_e n_e \boldsymbol{E} \cdot \boldsymbol{n}_s\right] - a\left(\frac{5}{2}k_b T_{\text{se}}\right)\sum_k \gamma \boldsymbol{J}_{+k,s} \cdot \boldsymbol{n}_s \tag{11}$$

where the secondary electron emission coefficient $\gamma$ is taken to be 0.05, following [34]. The temperature of secondary electrons ejected from the electrode surface $T_{se}$ is assumed to be 1 eV [34]. In Eqs. (8–11), $a = 1$ if $\boldsymbol{E} \cdot \boldsymbol{n}_s < 0$, and $a = 0$ otherwise.

A zero flux boundary condition is also imposed for the mass and momentum conservation equations. Analytic self-similar solutions of transient temperature distribution in a semi-infinite solid with a constant heat flux [35] are used as the boundary condition for the gas temperature,

$$T_b = \frac{T_{amb} + G(t) \times T_{gw}}{1 + G(t)}; \qquad G(t) = \frac{4k_{gw}\sqrt{\alpha_d t/\pi}}{k_d \Delta x} \qquad (12)$$

where the thermal conductivity of quartz $k_d$ is 1.4 W·m⁻¹·K⁻¹. In practice, this boundary is closer to isothermal than adiabatic conditions.

### C. Fitting of Voltage Waveform

In the simulations, a Gaussian fit of the experimental high-voltage pulse waveform is used, as shown in Fig. 2. Note that the curve fit used in the present simulations uses only two voltage peaks, whereas the measured waveform has additional smaller peaks. It is found that the input energy coupled after the first two peaks of the voltage waveform is negligible, so the latter peaks are neglected in the simulation in order to improve computational efficiency. To tackle the multiscale nature of the problem, adaptive time stepping is implemented with small time steps $(10^{-13} - 10^{-12}$ s) during each voltage pulse and larger time steps $(10^{-10}$ s) in the gap between two consecutive pulses. More details about the numerical methods can be found in the work by Nagaraja et al. [30,31] and Yang et al. [36].

### D. Transport Coefficients of Electron and Rate Coefficients of Electron Impact Reactions

The electron reaction rate and transport coefficients are fitted as functions of electron energy calculated by computer program BOLSIG [37] and renewed at every time step via interpolation. The electron impact dissociation, ionization, and excitation reaction rate constants are also calculated using BOLSIG and expressed as functions of electron energy. For this purpose, most of the impact cross-sections is obtained from the LXCat databases [38–41]. The $C_2H_4$ excitation cross-sections are estimated based on Janev and Reiter's method [42].

### E. $C_2H_4/O_2/Ar$ Plasma Chemistry Mechanism

The plasma combustion chemistry mechanism used in the present work is a recently developed low-temperature (below 700–800 K) plasma combustion mechanism (combining HP-Mech and an associated plasma submechanism) [25]. A combination of USC Mech-II [26] and the same plasma submechanism is also used [32], for comparison, to examine the effect of kinetic mechanisms. The rate constants of reactions between an excited Ar atom (Ar*) and ground state $O_2$ molecules are taken from Sun et al. [43]. Previous studies

[44,45] showed that the dominant reaction pathway for atomic oxygen generation is e + O₂ = e + O + O(¹D), which means that almost half of the atomic oxygen produced by plasma is O(¹D). Table 1 lists the production reactions of O(¹D) [44–46]. O(¹D) can subsequently react with $O_3$ [45] (Table 2), be quenched [43,45,47] (Table 3), or react with hydrocarbons [48–54] (Table 4). It was previously believed that O(¹D) reactions with hydrocarbons are not significant, due to their fast quenching reactions with the diluent gases [24,25], so most of the available plasma chemistry mechanisms do not contain reactions between O(¹D) and hydrocarbons. In typical plasma-assisted combustion environments, however, the concentrations of hydrocarbons are high, and the rate of reactions between O(¹D) and hydrocarbons may not be negligible [29]. In this study, reactions between O(¹D) and hydrocarbons are added to the kinetic mechanism (Table 4).

## IV. Results and Discussion

### A. Electrical Characteristics

Figure 3 shows the input energy per pulse as a function of pulse number. During the early stages, a significant increase in the ionization rate makes it easier to pump in energy, so the input energy per pulse increases with pulse number. After approximately 50 pulses, the composition reaches quasi equilibrium, and the input energy per pulse levels off at approximately 0.7 mJ.

Figure 4 illustrates the time variation of the reduced electric field (E/N) at the center of the discharge gap and input energy during the 1st pulse (early stage) and the 50th pulse (quasi equilibrium), respectively, as predicted by the present model. The E/N profile shows a sharp increase at around 5–10 ns, reaching a peak value of about 300 Td. At this juncture, electrical breakdown occurs in the gap, and sheath formation shields the electric field from further increases with applied voltage, as can also be observed from the gap voltage shown in Fig. 2. As a consequence, the electric field rapidly drops to zero. The high E/N values during the voltage pulse indicate high electron energy fluxes and suggest that a significant fraction of the input pulse energy is consumed in electron impact dissociation, excitation, and ionization reactions [55]. This effect results in efficient production of radical species such as O, H, and OH as well as fuel fragments such as $C_2H_3$, $C_2H_2$, and $CH_4$ and several excited states of O, $O_2$, and Ar, including O(¹D, ¹S), $O_2(a^1\Delta_g, b^1\Sigma_g^+, c^1\Sigma_u^-)$, and Ar*. For the first pulse, input energy during breakdown is 0.5 mJ, and total input energy per pulse is 0.65 mJ. Thus, breakdown accounts for 77% of the total input energy, which is the same as in the hydrogen/air plasma discharge simulation [31]. The majority of the remaining 23% of input energy is added by the secondary spike of the voltage pulse. For the 50th pulse, input energy during breakdown is 0.525 mJ, and the total input energy per pulse increases to 0.7 mJ. Thus, breakdown accounts for 75% of the total energy, and 25% of the input energy is deposited by the secondary spike of the voltage pulse. In contrast, the 0D simulation [25] uses a square waveform for E/N with a 12 ns width and 350 Td peak value. Neither the width nor the peak value is accurate, and this contributes to the significant overprediction of the gas temperature by the 0D model.

Figure 5a shows the electron number density at the center of the domain as a function of time. Note that the fluctuations in Fig. 5a come from the 150 high frequency periodical voltage pulses. The peak electron number density is approximately $2 \times 10^{12}$ cm⁻³ for all pulses, which is of the same order as the hydrogen/air discharge simulations [31], and efficiently produces radical species. Figure 5b shows the spatial distribution of electron number density of the 1st, 15th, 50th, 100th, and 150th pulses. The electron profiles are flat with a small gradient (variation between $x = 0.2$ cm and $x = 1.2$ cm is within 25%), except for sharp spikes in the sheath layers. This indicates uniform discharge in the bulk plasma region, which in turn implies that the heat release and radical generation would also be uniform in the bulk plasma region. The spatial data are collected only at the end of each pulse, and the overlapping of curves of different pulses in Fig. 5b indicates the periodic behavior of the electron number density. The spatial data are collected after the negative secondary spike in the voltage (see Fig. 2). Negative voltage means that the left electrode
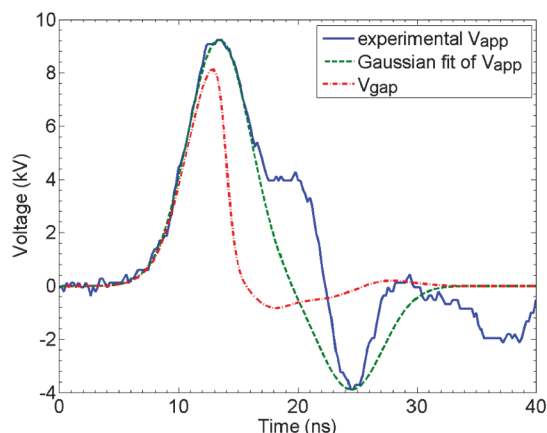


**Fig. 2 Gaussian fit to experimental pulse waveform used in simulation.**

**Table 1  Production reactions of O($^1$D)**

| No. | Reactions | Reaction rate constant (cm$^3 \cdot$ mol$^{-1} \cdot$ s$^{-1}$) | Reference |
|---|---|---|---|
| 1.a | e + O$_2$ = e + O + O($^1$D) | $f(E/N)$ | [44] |
| 1.b | e + O$_2^+$ = O + O($^1$D) | $1.62 \times 10^{17} \times (300/T_e)^{0.7} \times 0.40$ | [45] |
| 1.c | O$_2(a^1\Delta_g)$ + O$_3$ = O$_2$ + O$_2$ + O($^1$D) | $3.13 \times 10^{13} \times \exp(-2840/T_{gas})$ | [45] |
| 1.d | O$_2(b^1\Sigma_g^+)$ + O = O$_2$ + O($^1$D) | $3.62 \times 10^{13} \times (T_{gas})^{-0.1} \times \exp(-4200/T_{gas})$ | [45] |
| 1.e | O($^1$S) + O = O($^1$D) + O | $3.01 \times 10^{13} \times \exp(-300/T_{gas})$ | [46] |
| 1.f | O($^1$S) + O$_2$ = O($^1$D) + O$_2$ | $7.83 \times 10^{11} \times \exp(-850/T_{gas})$ | [46] |
| 1.g | O($^1$S) + O$_2(a^1\Delta_g)$ = O($^1$D) + O$_2(b^1\Sigma_g^+)$ | $1.75 \times 10^{13}$ | [46] |
| 1.h | O($^1$S) + O$_3$ = O$_2$ + O + O($^1$D) | $1.75 \times 10^{14}$ | [46] |

**Table 2  Reactions between O($^1$D) and O$_3$**

| No. | Reactions | Reaction rate constant (cm$^3 \cdot$ mol$^{-1} \cdot$ s$^{-1}$) | Reference |
|---|---|---|---|
| 2.a | O($^1$D) + O$_3$ = O$_2$ + O + O | $7.22 \times 10^{13}$ | [45] |
| 2.b | O($^1$D) + O$_3$ = O$_2$ + O$_2$ | $7.22 \times 10^{13}$ | [45] |

**Table 3  Quenching reactions of O($^1$D)**

| No. | Reactions | Reaction rate constant (cm$^3 \cdot$ mol$^{-1} \cdot$ s$^{-1}$) | Reference |
|---|---|---|---|
| 3.a | O($^1$D) + O = O + O | $4.82 \times 10^{12}$ | [45] |
| 3.b | O($^1$D) + O$_2$ = O + O$_2$ | $3.85 \times 10^{12} \times \exp(67/T_{gas})$ | [45] |
| 3.c | O($^1$D) + O$_2$ = O + O$_2$ ($a^1\Delta_g$) | $6.02 \times 10^{11}$ | [45] |
| 3.d | O($^1$D) + O$_2$ = O + O$_2$ ($b^1\Sigma_g^+$) | $1.57 \times 10^{13} \times \exp(67/T_{gas})$ | [45] |
| 3.e | O($^1$D) + Ar = Ar + O | $6.02 \times 10^{10}$ | [43] |
| 3.f | C$_2$H$_6$ + O($^1$D) = C$_2$H$_6$ + O | $4.40 \times 10^{14}$ | [47] |

**Table 4  Reactions between O($^1$D) and hydrocarbons**

| No. | Reactions | Reaction rate constant (cm$^3 \cdot$ mol$^{-1} \cdot$ s$^{-1}$) | Reference |
|---|---|---|---|
| 4.a | O($^1$D) + H$_2$ = H + OH | $6.62 \times 10^{13}$ | [48] |
| 4.b | CH$_4$ + O($^1$D) = CH$_3$ + OH | $6.80 \times 10^{13}$ | [49] |
| 4.c | CH$_4$ + O($^1$D) = CH$_2$O + H$_2$ | $4.52 \times 10^{12}$ | [49] |
| 4.d | CH$_4$ + O($^1$D) = CH$_3$O + H | $1.81 \times 10^{13}$ | [49] |
| 4.e | CH$_4$ + O($^1$D) = CH$_3$OH | $2.99 \times 10^{13}$ | [54] |
| 4.f | C$_2$H$_4$ + O($^1$D) = C$_2$H$_3$ + OH | $3.04 \times 10^{13}$ | [50,51][a] |
| 4.g | C$_2$H$_4$ + O($^1$D) = CH$_3$ + HCO | $7.13 \times 10^{13}$ | [50,51][a] |
| 4.h | C$_2$H$_4$ + O($^1$D) = CH$_2$ + CH$_2$O | $3.04 \times 10^{13}$ | [50,51][a] |
| 4.j | C$_2$H$_6$ + O($^1$D) = C$_2$H$_5$OH | $5.99 \times 10^{14}$ | [54] |
| 4.i | C$_2$H$_6$ + O($^1$D) = C$_2$H$_5$ + OH | $3.78 \times 10^{14}$ | [52] |
| 4.k | HO$_2$ + O($^1$D) = OH + O$_2$ | $4.00 \times 10^{13}$ | Estimated[b] |
| 4.l | CO + O($^1$D) = CO$_2$ | $4.81 \times 10^{13}$ | [53] |

[a]The sum of reaction rate constants of reactions 4.f–4.h is provided by Kajimoto and Fueno [50], and the branching fraction for reaction 4.g was measured by Miyoshi et al. [51]. The branching fractions of reactions 4.f and 4.h are assumed to be equal due to the lack of data.

[b]The reaction rate constant of reaction 4.k is estimated to be the same as HO$_2$ + O = OH + O$_2$ due to the lack of data.

becomes the anode, which attracts more negative charges. For this reason, the electron number density is higher near the left electrode than near the right electrode.

## B. Spatial Distribution

Figure 6 presents the spatial distribution of C$_2$H$_2$, CH$_4$, H$_2$O, and gas temperature at the 1st, 15th, 50th, 100th, and 150th pulses. The concentration profiles outside of the sheath regions are flat, so it is reasonable to use the values at the center of the domain for comparison with the average values measured in the experiment. These results also confirm that relatively stable fuel fractions and product species fractions are generated uniformly in the discharge volume, due to the homogeneity of the plasma discharge. In the sheath regions, reactions progress faster than in the bulk plasma, especially during the earlier pulses, owing to the accumulation of high-energy electrons and ions, resulting in large gradients in species concentrations. Gas temperature rises uniformly, which means that the plasma discharge provides essentially homogeneous heating for the gas mixture via both Joule

heating and heat release from reactions. This also justifies the assumption of uniform temperature in the diode laser absorption. It can also be observed that the boundary is very close to isothermal conditions; this is due to the short time scales of the present study. The local Joule heating rate is equal to the dot product of the local electric field and the local charge flux. Simulation results indicate that if all of the Joule heating became direct gas heating, the temperature rise would be significant only inside the sheath layers because the electric field is only significant there, and its energy input would quickly be lost to the walls due to the quasi-isothermal boundary condition. In addition, even if the wall were adiabatic, the heat conduction process would be too slow to increase the gas temperature at the center of the reactor. Thus, direct gas heating through electron/neutral species momentum transfer collision is not the primary source of the temperature increase at the center of the reactor; heat release from reactions is the primary source. The 0D model assumes that all Joule heating is completely converted to a temperature rise, and this contributes to the significant overprediction of temperature by the 0D model [25].
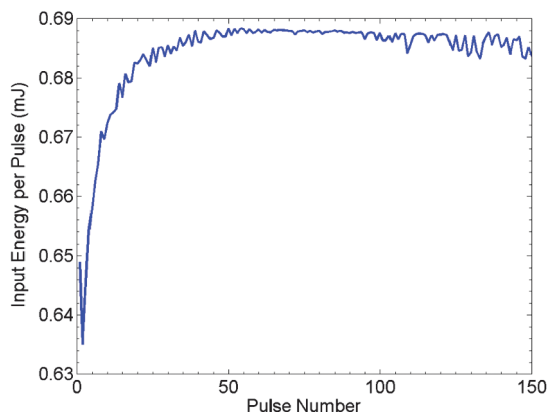
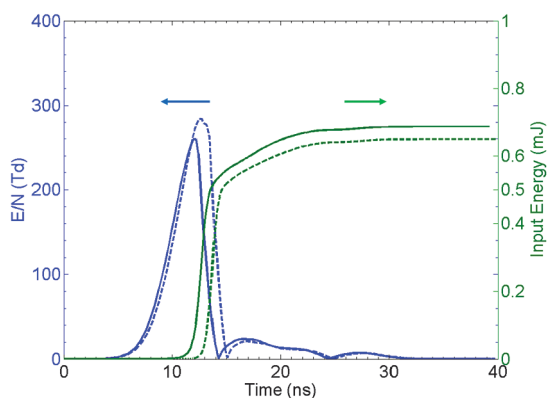**Fig. 3    Input energy per pulse as a function of pulse number.**



**Fig. 4    Time variation of reduced electric field (E/N) at center of discharge gap and input energy during 1st pulse (early stage: dashed line) and 50th pulse (quasi-equilibrium: solid line).**
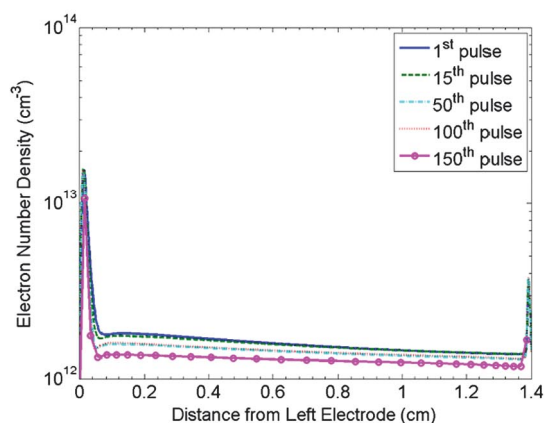


a)



b)

**Fig. 5    a) Electron number density at center of domain as function of time. b) Spatial distribution of electron number density.**

### C.    Comparison of 1D Model, 0D Model, and Experiment

The modeling results from the 1D and the 0D models [24,25], using HP-Mech, are compared with the experimental data in Fig. 7. It is observed that the trends of the numerical and experimental results agree well, but for all quantities, the 1D model provides better prediction than the 0D model. Both the $H_2O$ and the $CH_4$ concentrations from the 1D model fall within the uncertainty range of the experimental measurements and are significantly closer to the experimental results than those of the 0D model.

Since the HP-Mech plasma combustion chemistry mechanism is employed in both the 1D and 0D models, the observed discrepancies in the results must originate from the differences in the physical models (sheath formation and accurately calculated E/N) and the reactions between $O(^1D)$ and hydrocarbons. The $C_2H_2$ concentration from the 1D model is within a factor of 2 of the experimental data and is 11% closer to experimental data than the 0D model. Compared to the experimental data, the 1D model underpredicts the gas temperature, while the 0D model overpredicts the gas temperature. The discrepancies are both significant, but the 1D model result is 10% closer to experimental data. Actually, most energy is consumed in either breaking the chemical bonds or depositing into excited states, and direct gas heating is negligible at the center of the discharge gap (see the previous sections). Judging by the measured $H_2O$ concentration and the lack of $CO_2$ in the steady-state measurements [25], the heat release from chemical reactions (including the recombination of radicals) and quenching of excited states with neutrals ("fast gas heating effect" [56]) is not significant enough to compensate, the input energy to break the chemical bond or depositing into excited states. In the present low-temperature environment, most reaction rates are not sensitive to temperature, and the temperature deviation has a negligible effect on the prediction of species evolution.
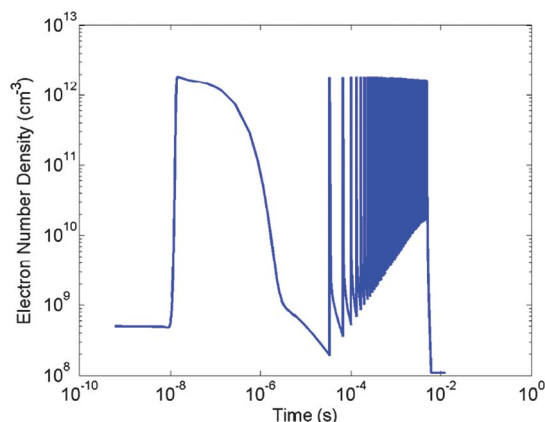
To demonstrate the difference between the 1D and 0D models, Figs. 8 and 9 present the path flux analysis of $C_2H_4$ oxidation based on carbon atoms at a 60 torr pressure and 300 K initial temperature for the 1D and 0D models [25], respectively. In both Figs. 8 and 9, for any species, if the inlet fluxes are much larger than the outlet fluxes, the outlet pathways are not listed. For example, the Waddington sequence [57] for the decomposition of $O_2C_2H_4OH$ is neglected in the 1D model also. In addition, consumption fluxes of $C_2H_4$ with less than 1% contribution are also not listed in the figures. It can be seen from both Figs. 8 and 9 that plasma activates the pathways of $C_2H_4$ oxidation, which cannot occur without plasma. There are three primary fuel consumption pathways: 1) a plasma-activated low-temperature fuel oxidation pathway involving $O_2$ addition to the fuel radicals, leading to $C_2H_5O_2$ or $O_2C_2H_4OH$; 2) direct fragmentation pathways via collisional dissociation by electrons, ions, and electronically excited molecules; and 3) a direct oxidation pathway by plasma-generated radicals and excited molecules. In pathway 1, the inlet flux of $C_2H_5O_2$ is much stronger than its outlet flux in the 1D simulation, but a significant amount of $C_2H_5O_2$ is converted into $C_2H_5O_2H$ in the 0D simulation. $O_2C_2H_4OH$ is relatively stable in the 1D simulation but decomposes to two $CH_2O$ molecules and an OH (the Waddington sequence [57]) in the 0D simulation. This may be due to the significant overprediction of the gas temperature in the 0D model. The Waddington sequence is the principal cause of the formation of $CH_2O$ in the 0D simulation, while nearly ten other reactions, with none dominant, contribute to the $CH_2O$ in the 1D simulation. In the 0D simulation, pathway 1 is found to be dominant. Pathway 2 dominates in the 1D simulation; 73% of the $C_2H_4$ consumption is due to pathway 2, primarily during the breakdown of each pulse. In particular, about 48% of $C_2H_4$ is converted to $C_2H_2$ directly rather than through the pathway of $C_2H_4 \rightarrow C_2H_3 \rightarrow C_2H_2$ (which dominates in the absence of plasma discharge). This leads to more $C_2H_2$ formation and accumulation than in the 0D model, as
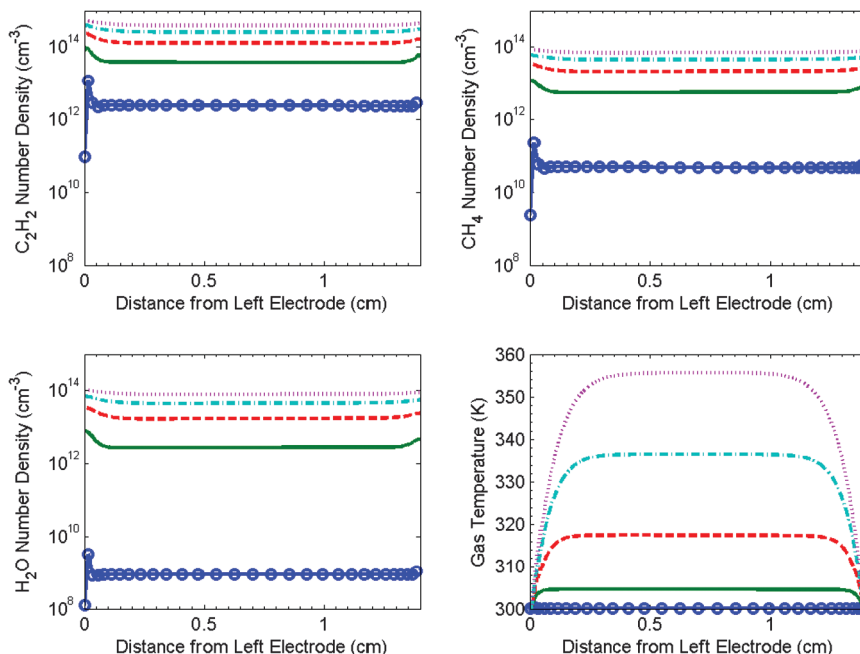
**Fig. 6  Spatial distribution of $C_2H_2$, $CH_4$, $H_2O$, and gas temperature. Blue solid line with circle: 1st pulse; green solid line: 15th pulse; red dashed line: 50th pulse; cyan dashed-dotted line: 100th pulse; magenta dotted line: 150th pulse.**
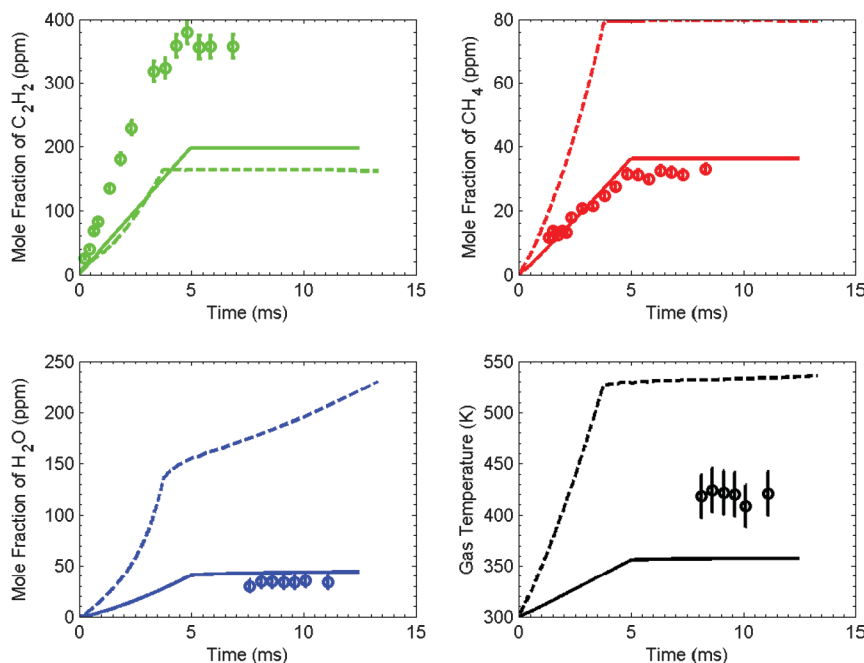


**Fig. 7  Comparison of 1D model (solid line), 0D model (dashed line), and experiment (circle) for the formation of $C_2H_2$, $CH_4$, $H_2O$, and gas temperature.**

shown in Fig. 7. In particular, 86% of $C_2H_2$ is generated from electron impact dissociation reactions, while its consumption is negligible, even during the gap between pulses. Considering the factor of 2 error in the $C_2H_2$ concentration, the reaction rates of these electron impact dissociation reactions might still be too low. For the same reason, about 15% of $C_2H_4$ is converted to $C_2H_3$ via an electron impact dissociation reaction followed by $\beta$-scission, which contributes about 85% of the $C_2H_3$ formation. Significant amounts of H and OH are also generated during the previously mentioned reactions. In addition, electron impact reactions and $Ar^+$ charge exchange reactions generate several new pathways: $C_2H_4$ can be ionized to $C_2H_3^+$ and $C_2H_2^+$, which will then recombine with $O_2^-$ to $C_2H_2$ and $C_2H_3$ respectively. In pathway 3, excited species like $O(^1D)$ significantly enhance both H abstraction and dissociation reactions.

In particular, $C_2H_4 + O(^1D) = CH_3 + HCO$ contributes 19% of HCO and 60% of $CH_3$. This in turn significantly enhances hydrocarbon oxidation, since 83% of CO comes from HCO. In addition, $C_2H_3$ is rapidly consumed to form $CH_2O$, HCO, and CO during the gap between two pulses. As a result, the $C_2H_3$ concentration oscillates rather than constantly increasing from one pulse to the next pulse. Plasma discharge enables $C_2H_4$ oxidation under low temperature by creating new pathways for the more efficient oxidation of $C_2H_4$.

### D.  Comparison Between HP-Mech and USC Mech-II Predictions of 1D Model and Experiment

Use of an appropriate kinetic mechanism is another key component in high-fidelity modeling of plasma-assisted oxidation
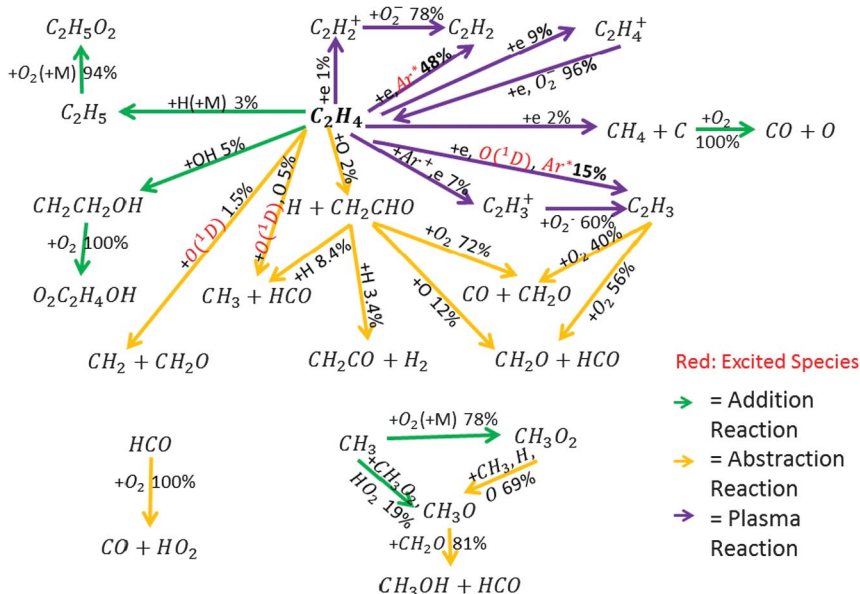
**Fig. 8   Path flux analysis for hydrocarbon fuel oxidation based on carbon element at $p = 60$ torr pressure and $T = 300$ K initial temperature for 1D model.**
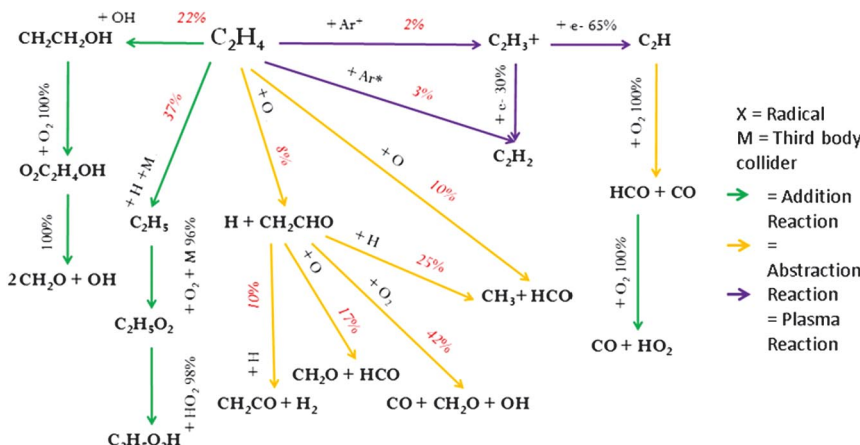


**Fig. 9   Path flux analysis for hydrocarbon fuel oxidation based on carbon element at $p = 60$ torr pressure and $T = 300$ K initial temperature for 0D model (from Lefkowitz et al. [25]).**

and combustion. Figure 10 shows a comparison of the HP-Mech and USC Mech-II 1D numerical models with experimental data for the formation of the major intermediate species, $C_2H_2$, $CH_4$, major product $H_2O$, and gas temperature. It is observed that the trends of the numerical and experimental results agree well. For both $H_2O$ and $CH_4$, HP-Mech provides better predictions than USC Mech-II. In particular, $H_2O$ concentration from USC Mech-II is more than 25 times larger than the results of either HP-Mech or the experiment. Furthermore, both $H_2O$ and $CH_4$ concentrations from HP-Mech fall into the uncertainty range of the experimental measurements. For $C_2H_2$, there is no observable difference between the two mechanisms, and both are within a factor of 2 of the experimental data. Both simulations predict similarly low gas temperature compared to the experimental data.

To further demonstrate the difference between HP-Mech and USC Mech-II, the time evolution of $CH_3$ and OH is presented in Fig. 11. A pathway comparison of the two mechanisms is presented in Fig. 12. With USC Mech-II, both $CH_3$ and OH increase to high quasi-equilibrium concentrations during the plasma discharge, while they oscillate at low concentrations with HP-Mech. In USC Mech-II, more than half of the $CH_3$ consumption is from the $CH_3 + HO_2 \rightarrow CH_3O + OH$ pathway. In contrast, HP-Mech exclusively contains the species $CH_3O_2$ and a notably faster pathway $CH_3 \rightarrow CH_3O_2$, which contributes to 78% of the $CH_3$ consumption. For this reason, $CH_3$ is rapidly consumed in HP-Mech during the gap between two

pulses and oscillates periodically from one pulse to the next. Furthermore, USC Mech-II exclusively contains a relatively faster pathway of $C_2H_5 \rightarrow CH_3 + CH_2O$ to generate more $CH_3$, which is replaced by $C_2H_5 \rightarrow C_2H_5O$ in HP-Mech. The $C_2H_5$ in $C_2H_5 \rightarrow CH_3 + CH_2O$ primarily comes from the fast third-body reaction $C_2H_4 + H(+M) = C_2H_5(+M)$. In contrast, in HP-Mech, $CH_3$ is primarily generated from two slower reactions $C_2H_4 + (O(^1D), O) = CH_3 + HCO$, the contributions of which are small in USC Mech-II. In summary, in USC Mech-II, $CH_3$ has a faster production rate through the $C_2H_4 \rightarrow C_2H_5 \rightarrow CH_3 + CH_2O$ reaction pathway, and slower consumption rate through $CH_3 + HO_2 \rightarrow CH_3O + OH$, which results in its continuous increase. In HP-Mech, $CH_3$ has a slower generation rate, from $C_2H_4 \rightarrow CH_3 + HCO$, and a faster destruction rate, from $CH_3 \rightarrow CH_3O_2$, which together result in its oscillating behavior at low concentrations.

In USC Mech-II, nearly half of the $CH_4$ formation is from the high level of $CH_3$, mainly assisted by $HO_2$. In contrast, this pathway only contributes to 11% of the $CH_4$ formation in HP-Mech, due to the low concentration of $CH_3$. In addition, the electron impact reaction $e + C_2H_4 = e + C + CH_4$ (see Fig. 8) contributes 82% of $CH_4$ in HP-Mech but only about half of $CH_4$ in USC Mech-II. As a result, the concentration of $CH_4$ in HP-Mech is lower than that in USC Mech-II, as shown in Fig. 10. Note that the 0D simulation [25] produces completely different results: methane is underpredicted by USC Mech-II and overpredicted by HP-Mech, probably due to the inaccu-
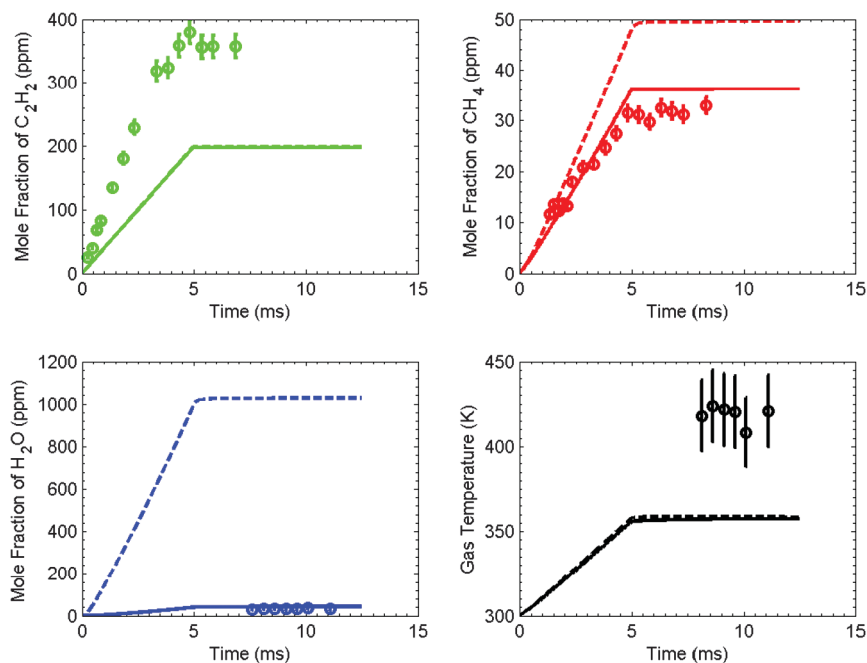
**Fig. 10   Formation of $C_2H_2$, $CH_4$, and $H_2O$ and gas temperature: HP-Mech (solid line), USC Mech-II (dashed line), and experiment (circle).**
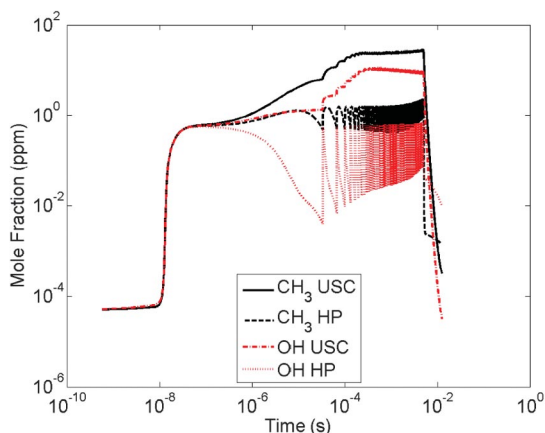


**Fig. 11   Comparison of USC Mech-II and HP-Mech: formation of $CH_3$ and OH at center of discharge gap.**

rate electron energy prediction in the 0D model and subsequent competition from other reaction pathways. The consumption of $CH_4$ shown in Fig. 8 is very weak, even during the gap between two pulses, so it increases with the number of pulses for both kinetic mechanisms.

Because of the high concentration of $CH_3$, the rate of $CH_3 + HO_2 \rightarrow CH_3O + OH$ in USC Mech-II is much higher than the corresponding reaction rate in HP-Mech, which generates much more OH. More precisely, it constitutes 59% of OH generation in USC Mech-II, such that OH increases to a high concentration quasi equilibrium rather than oscillating periodically at low concentration. In contrast, 63% of OH generation in HP-Mech relies on two relatively slow reactions, $CH_2CHO + O_2 = CO + CH_2O + OH$ and $C_2H_4 + O(^1D) = C_2H_3 + OH$, the contributions of which are minor in USC Mech-II. These reactions result in the periodic behavior of OH at low concentration. In USC Mech-II, 83% of OH is converted to $H_2O$, which contributes to 95% of the $H_2O$ formation. In contrast, HP-Mech has a significantly lower OH level, and 90% of OH is combined with $C_2H_4$ to form $CH_2CH_2OH$ (collisionally stabilized 2-hydroxyethyl radical) rather than $H_2O$. $CH_2CH_2OH$ then combines with $O_2$ to form $O_2C_2H_4OH$. Both $CH_2CH_2OH$ and $O_2C_2H_4OH$ are relatively stable in the present low-temperature

environment within the time scales of interest, so very little dissociation and OH recovery occur. As a result, the $H_2O$ concentration in HP-Mech is more than 25 times lower than that in USC Mech-II. In contrast, even HP-Mech greatly overpredicts $H_2O$ concentration in the 0D simulation [25] (see Fig. 7).

In summary, HP-Mech provides better predictions of species concentrations than USC Mech-II for the present low-temperature condition. For this reason, only HP-Mech is used in the remaining sections of this work. In addition, the 1D simulation results suggest that the large discrepancy between the 0D model [25] predictions with HP-Mech and the experimental data is probably due to missing physical structures (sheath formation and accurately calculated E/N) rather than the inaccuracy of the kinetic model.

### E.   Time Evolution of Active Species

The previously mentioned results show that a significant fraction of the input pulse energy is consumed in electron impact reactions, which results in efficient production of radical species and several excited states of O, $O_2$, and Ar. These species are the primary source of plasma-activated oxidation, so it is important to study their evolution over time, and their reaction pathways.

Figure 13a shows the time variation of mole fractions of radicals H, O, OH, and $HO_2$ at the center of the discharge gap. The time evolution of H, O, and OH during the first pulse and first time period (between the beginnings of the first and second pulses) is shown in Fig. 13b. There is a sharp increase in mole fractions of H, O, and OH in the time interval of 7–13 ns, while $HO_2$ only starts to increase gradually. The sharp rise of H and O is primarily due to fast electron impact reactions with 58% of H generation coming from $e + C_2H_4 = e + (C_2H_3, C_2H_2 + H) + H$ and 72% of O generation from $e + O_2 = e + O + O(^1D)$, which also generates equal amounts of $O(^1D)$. O increases before H does because of the higher concentration of $O_2$ relative to $C_2H_4$. The rise of OH is later because 63% of OH generation comes from $CH_2CHO + O_2 = CO + CH_2O + OH$ and $C_2H_4 + O(^1D) = C_2H_3 + OH$, which rely on the generation of $CH_2CHO$ from $C_2H_4 + O = H + CH_2CHO$ and $O(^1D)$ from $e + O_2 = e + O + O(^1D)$. In the present low-pressure environment, three-body recombination of H with $O_2$ molecules only contributes 3% of the $HO_2$ formation, whereas 89% of the $HO_2$ formation comes from $HCO + O_2 = CO + HO_2$. $HO_2$ generation is slower than H, O, and OH because of the slow HCO generation from fuel pyrolysis/decomposition. $HO_2$ accumulates continuously because of the high level of oxygen and the continuous generation of HCO.
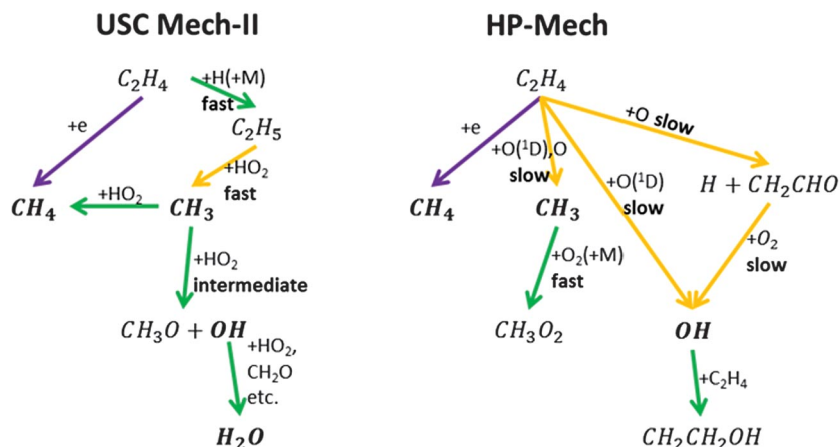
**Fig. 12    Comparison of USC Mech-II and HP-Mech via path flux analysis for related species at center of discharge gap.**

Also, $HO_2$ is quasi-stable and reacts much slower than the other radicals at these low temperatures (see Fig. 13). After 150 pulses, most radicals are quenched to below 1 ppm, except $HO_2$, which has a relatively high concentration of 25.7 ppm.

Figure 14a illustrates the time evolution of the mole fractions of excited Ar atoms ($Ar^*$), excited atomic oxygen including $O(^1D, {}^1S)$, and excited $O_2$ including $O_2(a^1\Delta_g, b^1\Sigma_g^+, c^1\Sigma_u^-)$ at the center of the gap. Most of these excited species show a sharp increase during the breakdown of each pulse, mainly due to electron impact excitation reactions. After the sharp increase in the first pulse, the $O_2(a^1\Delta_g, b^1\Sigma_g^+)$ concentration is almost constant, until it increases

further during the breakdown of the next pulse because of the new energy input. $Ar^*$, $O(^1S)$, and $(O_2(c^1\Sigma_u^-))$ gradually drop until the next pulse, primarily due to quenching reactions and converting pathways of $O(^1S) \rightarrow O(^1D)$ and $O_2(c^1\Sigma_u^-) \rightarrow O_2(b^1\Sigma_g^+) \rightarrow O_2(a^1\Delta_g)$. $O(^1D)$ also gradually drops until the next pulse, primarily due to the reactions with hydrocarbons listed in Table 4. The effects of $O(^1D)$ reactions will be discussed in detail in Sec. IV.F. $O(^1S)$ has a much smaller production rate than $O(^1D)$, as shown in Fig. 14a, so its reactions with hydrocarbons are not included in the present model. Consequently, the consumption rate of $O(^1S)$ is slower than that of $O(^1D)$ in the model. Globally, $O_2(a^1\Delta_g, b^1\Sigma_g^+)$ begins to accumulate, while the concentrations of $Ar^*$, $O(^1D^1S)$, and $O_2(c^1\Sigma_u^-)$ oscillate
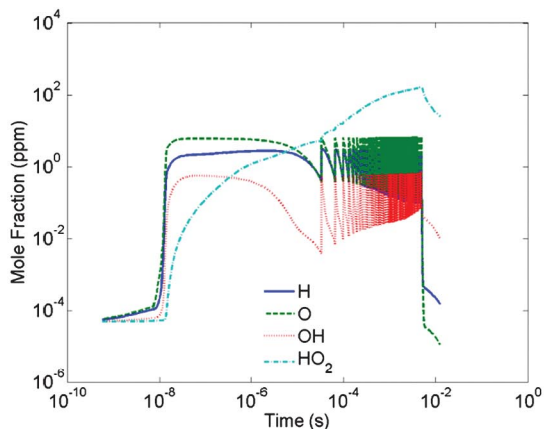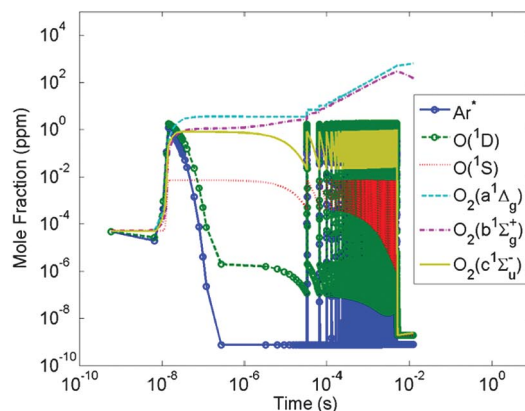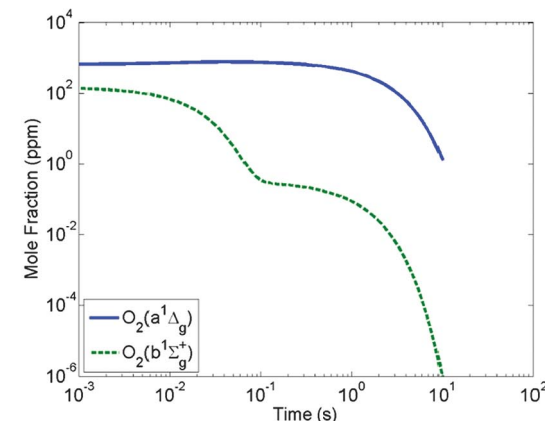


a)
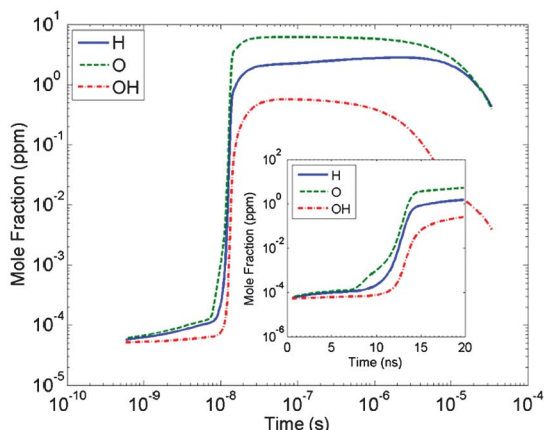


b)

**Fig. 13    a) Time evolution of mole fractions of H, O, OH, and $HO_2$ radicals at center of domain. b) Time evolution of H, O, and OH during first discharge pulse and first time period (between the beginning of first pulse and beginning of second pulse) at center of domain.**



a)



b)

**Fig. 14    a) Time evolution of mole fractions of excited O atoms: $O(^1D)$, $O(^1S)$, and excited $O_2$: $O_2(a^1\Delta_g)$, $O_2(b^1\Sigma_g^+)$, $O_2(c^1\Sigma_u^-)$. b) Decay of $O_2(a^1\Delta_g)$ and $O_2(b^1\Sigma_g^+)$ after 150 pulses.**

**Table 5  Comparison of species concentrations between cases with (new) and without (old) O($^1$D) reacting with hydrocarbons at the end of the simulation**

| ppm | H$_2$O | CH$_3$CHO | CH$_2$CHO | CH$_2$CO | O$_2$C$_2$H$_4$O | CH$_4$ | CH$_2$O | CO$_2$ | O$_2(a^1\Delta_g)$ | O$_2(b^1\Sigma_g^+)$ |
|---|---|---|---|---|---|---|---|---|---|---|
| New | 44 | 11 | 22 | 42 | 595 | 36 | 325 | 70 | 647 | 148 |
| Old | 33 | 12 | 28 | 48 | 504 | 41 | 250 | 38 | 750 | 229 |
| Diff., % | 33 | 11 | 19 | 14 | 18 | 11 | 30 | 82 | 14 | 35 |

periodically. The concentration of O$_2$(O$_2(a^1\Delta_g)$, $b^1\Sigma_g^+$) is still high at the end of 150 pulses. This is because 95% of the decay of O$_2(a^1\Delta_g)$ and 37% of that of O$_2(b^1\Sigma_g^+)$ rely on the low concentration species O$_2^-$, O$_3$, and C$_2$H.

Figure 14b shows the decay of O$_2(a^1\Delta_g)$ and O$_2(b^1\Sigma_g^+)$ as calculated by the 0D homogeneous reactor in CHEMKIN-PRO [58], using the calculated composition and temperature of the gas mixture at the center of the discharge gap after 150 pulses as the initial conditions. The long characteristic decay times of O$_2(a^1\Delta_g)$ and O$_2(b^1\Sigma_g^+)$ are 6.7 and 0.0329 s, respectively, at 60 torr. Such characteristic decay times are too long for accurate 1D simulation, so fast 0D simulation is adopted here to get an understanding of approximately how long it would take for these species to decay at the present conditions and to justify the building up of these species in the full 1D calculations. As there is no plasma discharge in this test, the inaccuracies of the 0D model are not relevant here.

### F.  Significance of O($^1$D) Reacting with Hydrocarbons

Path flux analysis shows that only 19% of O($^1$D) quenches to O, but 80% of O($^1$D) reacts with hydrocarbons. This result clearly indicates that the dominant reaction pathways of O($^1$D) are the reactions with hydrocarbons. Table 5 lists ten species of which the mole fractions are more than 10 ppm and shows a significant difference the between cases with (new) and without (old) the reactions of O($^1$D) with hydrocarbons (Table 4) after 150 pulses. Some transient species like OH, with very low final concentrations, are not included in this table. (Note that all the other simulation results presented here include reactions of O($^1$D) with hydrocarbons.) About 24% of OH is generated from reaction C$_2$H$_4$ + O($^1$D) = C$_2$H$_3$ + OH. As a result, H$_2$O rises, primarily due to the enhancement of two reactions (HO$_2$, C$_2$H$_4$) + OH = (O$_2$, C$_2$H$_3$) + H$_2$O for product generation. Concentrations of H$_2$ and CO are high, while that of O($^1$D) is relatively low, so H$_2$ and CO are almost unaffected by these newly added reactions between O($^1$D) and hydrocarbons. As in Fig. 8, 63% of CH$_2$ and 17% of CH$_2$O result directly from C$_2$H$_4$ + O($^1$D) = CH$_2$ + CH$_2$O. This in turn contributes 53% of the CO$_2$ formation via CH$_2$ + O$_2$ = CO$_2$ + (H + H, H$_2$).

## V.  Conclusions

Numerical and experimental efforts are combined to investigate the effect of low-temperature, nanosecond pulsed, nonequilibrium plasma discharges on the oxidation of C$_2$H$_4$/O$_2$/Ar mixtures at 60 torr. A time-accurate one-dimensional (1D) model based on a two-temperature framework with a detailed chemistry/plasma mechanism is used to simulate the species and temperature evolution across the discharge gap. Simulation results from the 1D model are compared with those from previous implementation of a zero-dimensional (0D) model employing the same kinetic mechanism. It is shown that the 1D model can predict the experiments much more accurately than the 0D model; the 1D model is necessary for the proper interpretation of experimental results. The large discrepancy between the 0D simulation predictions and the experimental data is due to the absence of physical structures (sheath formation and accurately calculated E/N) rather than any inaccuracy in the kinetic model. The modeling results also show that direct gas heating is negligible outside of the sheath region, for the short time duration of the experiments.

Plasma discharge is proven to be homogenous in terms of the spatial distribution of both species and gas temperature, and this justifies the use of the values at the center of the domain to represent the average values measured in the experiment. It is found that the trends of the numerical and experimental results agree well. In particular, the numerical results for H$_2$O, C$_2$H$_2$, and CH$_4$ almost all fall within the uncertainty of the experimental measurements. The effect of the kinetic mechanism is investigated by running 1D simulations employing two different chemical kinetic mechanisms, HP-Mech and USC Mech II. HP-Mech provides significantly better predictions of CH$_4$ and H$_2$O concentrations than USC Mech-II, mainly because of the additional low-temperature C$_2$H$_4$ + OH = CH$_2$CH$_2$OH reaction in HP-Mech.

About 75–77% of the input pulse energy is consumed in electron impact dissociation, excitation, and ionization reactions. This results in efficient production of radicals, fuel fragments, and excited species. Generation of these reactive species is the major enhancement pathway of fuel oxidation. In particular, O and H are mainly generated by the electron impact dissociation of oxygen and C$_2$H$_4$, respectively, while 63% of OH generation comes from CH$_2$CHO + O$_2$ = CO + CH$_2$O + OH and C$_2$H$_4$ + O($^1$D) = C$_2$H$_3$ + OH. Reactions directly between O($^1$D) and hydrocarbons are proven to be very important and must be included when hydrocarbon concentration is high. H$_2$O and CO$_2$ formation are enhanced by the significant amount of OH generated from reactions between O($^1$D) and hydrocarbons. Furthermore, O($^1$D) reacting with C$_2$H$_4$ contributes 19% of HCO, 60% of CH$_3$, 63% of CH$_2$, and 17% of CH$_2$O. These in turn significantly enhance hydrocarbon oxidation, since 83% of CO comes from HCO and 53% of CO$_2$ comes from CH$_2$.

## References

[1] Sun, W., and Ju, Y., "Nonequilibrium Plasma-Assisted Combustion: A Review of Recent Progress," *Journal of Plasma and Fusion Research*, Vol. 89, No. 4, 2013, pp. 208–219.

[2] Ju, Y., and Sun, W., "Plasma Assisted Combustion: Progress, Challenges, and Opportunities," *Combustion and Flame*, Vol. 162, No. 3, 2015, pp. 529–532.
doi:10.1016/j.combustflame.2015.01.017

[3] Ju, Y., and Sun, W., "Plasma Assisted Combustion: Dynamics and Chemistry," *Progress in Energy and Combustion Science*, Vol. 48, No. 1, 2015, pp. 21–83.
doi:10.1016/j.pecs.2014.12.002

[4] Starikovskii, A. Y., Anikin, N., Kosarev, I., Mintoussov, E., Starikovskaia, S., and Zhukov, V., "Plasma-Assisted Combustion," *Pure and Applied Chemistry*, Vol. 78, No. 6, 2006, pp. 1265–1298.
doi:10.1351/pac200678061265

[5] Ombrello, T., and Ju, Y., "Kinetic Ignition Enhancement of H2 Versus Fuel-Blended Air Diffusion Flames Using Nonequilibrium Plasma," *IEEE Transactions on Plasma Science*, Vol. 36, No. 6, 2008, pp. 2924–2932.
doi:10.1109/TPS.2008.2005987

[6] Yang, S., Nagaraja, S., Sun, W., and Yang, V., "A Detailed Comparison of Thermal and Nanosecond Plasma Assisted Ignition of Hydrogen–Air Mixtures," *53rd AIAA Aerospace Sciences Meeting*, AIAA Paper 2015-1615, 2015.

[7] Nagaraja, S., Yang, V., Yin, Z., and Adamovich, I., "Ignition of Hydrogen–Air Mixtures Using Pulsed Nanosecond Dielectric Barrier Plasma Discharges in Plane-to-Plane Geometry," *Combustion and*

*Flame*, Vol. 161, No. 4, 2014, pp. 1026–1037.
doi:10.1016/j.combustflame.2013.10.007

[8]  Singleton, D., Pendleton, S. J., and Gundersen, M. A., "The Role of Non-Thermal Transient Plasma for Enhanced Flame Ignition in C2H4–Air," *Journal of Physics D: Applied Physics*, Vol. 44, No. 2, 2011, pp. 1–6.
doi:10.1088/0022-3727/44/2/022001

[9]  Lefkowitz, J. K., Guo, P., Ombrello, T., Won, S. H., Stevens, C. A., Hoke, J. L., Schauer, F., and Ju, Y., "Schlieren Imaging and Pulsed Detonation Engine Testing of Ignition by a Nanosecond Repetitively Pulsed Discharge," *Combustion and Flame*, Vol. 162, No. 6, 2015, pp. 2496–2507.
doi:10.1016/j.combustflame.2015.02.019

[10]  Starikovskaia, S., "Plasma Assisted Ignition and Combustion," *Journal of Physics D: Applied Physics*, Vol. 39, No. 16, 2006, p. R265.
doi:10.1088/0022-3727/39/16/R01

[11]  Leonov, S. B., and Yarantsev, D. A., "Plasma-Induced Ignition and Plasma-Assisted Combustion in High-Speed Flow," *Plasma Sources Science and Technology*, Vol. 16, No. 1, 2007, pp. 132–138.
doi:10.1088/0963-0252/16/1/018

[12]  Sun, W., Uddi, M., Ombrello, T., Won, S. H., Carter, C., and Ju, Y., "Effects of Non-Equilibrium Plasma Discharge on Counterflow Diffusion Flame Extinction," *Proceedings of the Combustion Institute*, Vol. 33, No. 2, 2011, pp. 3211–3218.

[13]  Pilla, G., Galley, D., Lacoste, D. A., Lacas, F., Veynante, D., and Laux, C. O., "Stabilization of a Turbulent Premixed Flame Using a Nanosecond Repetitively Pulsed Plasma," *IEEE Transactions on Plasma Science*, Vol. 34, No. 6, 2006, pp. 2471–2477.
doi:10.1109/TPS.2006.886081

[14]  Moeck, J., Lacoste, D., Laux, C., and Paschereit, C., "Control of Combustion Dynamics in a Swirl-Stabilized Combustor with Nanosecond Repetitively Pulsed Discharges," *51st AIAA Aerospace Sciences Meeting*, AIAA Paper 2013-0565, 2013.

[15]  Cha, M., Lee, S., Kim, K., and Chung, S., "Soot Suppression by Nonthermal Plasma in Coflow Jet Diffusion Flames Using a Dielectric Barrier Discharge," *Combustion and Flame*, Vol. 141, No. 4, 2005, pp. 438–447.
doi:10.1016/j.combustflame.2005.02.002

[16]  Oshia, H., Kimura, I., and Horisawa, H., "Control of Soot Emission of a Turbulent Diffusion Flame by DC or AC Corona Discharges," *Combustion and Flame*, Vol. 116, No. 4, 1999, pp. 653–661.
doi:10.1016/S0010-2180(98)00054-6

[17]  Sun, W., Won, S. H., Ombrello, T., Carter, C., and Ju, Y., "Direct Ignition and S-Curve Transition by in situ Nano-Second Pulsed Discharge in Methane/Oxygen/Helium Counterflow Flame," *Proceedings of the Combustion Institute*, Vol. 34, No. 1, 2013, pp. 847–855.

[18]  Kim, W., Do, H., Mungal, M. G., and Cappelli, M. A., "Optimal Discharge Placement in Plasma-Assisted Combustion of a Methane Jet in Cross Flow," *Combustion and Flame*, Vol. 153, No. 4, 2008, pp. 603–615.
doi:10.1016/j.combustflame.2007.11.015

[19]  Leonov, S. B., Yarantsev, D. A., Napartovich, A. P., and Kochetov, I. V., "Plasma-Assisted Combustion of Gaseous Fuel in Supersonic Duct," *IEEE Transactions on Plasma Science*, Vol. 34, No. 6, 2006, pp. 2514–2525.
doi:10.1109/TPS.2006.886089

[20]  Uddi, M., Jiang, N., Mintusov, E., Adamovich, I. V., and Lempert, W. R., "Atomic Oxygen Measurements in Air and Air/Fuel Nanosecond Pulse Discharges by Two Photon Laser Induced Fluorescence," *Proceedings of the Combustion Institute*, Vol. 32, No. 1, 2009, pp. 929–936.

[21]  Yin, Z., Adamovich, I. V., and Lempert, W. R., "OH Radical and Temperature Measurements During Ignition of H2-Air Mixtures Excited by a Repetitively Pulsed Nanosecond Discharge," *Proceedings of the Combustion Institute*, Vol. 34, No. 2, 2013, pp. 3249–3258.

[22]  Yin, Z., Montello, A., Carter, C. D., Lempert, W. R., and Adamovich, I. V., "Measurements of Temperature and Hydroxyl Radical Generation/Decay in Lean Fuel–Air Mixtures Excited by a Repetitively Pulsed Nanosecond Discharge," *Combustion and Flame*, Vol. 160, No. 9, 2013, pp. 1594–1608.
doi:10.1016/j.combustflame.2013.03.015

[23]  Mintusov, E., Serdyuchenko, A., Choi, I., Lempert, W. R., and Adamovich, I. V., "Mechanism of Plasma Assisted Oxidation and Ignition of Ethylene–Air Flows by a Repetitively Pulsed Nanosecond Discharge," *Proceedings of the Combustion Institute*, Vol. 32, No. 2, 2009, pp. 3181–3188.

[24]  Lefkowitz, J. K., Windom, B. C., MacDonald, W., Adams, S., Chen, T., Uddi, M., and Ju, Y., "Time Dependent Measurements of Species Formation in Nanosecond-Pulsed Plasma Discharges in C2H4/O2/Ar Mixtures," *AIAA Aerospace Science Meeting*, AIAA Paper 2014-1179, 2014.

[25]  Lefkowitz, J. K., Uddi, M., Windom, B., Lou, G. F., and Ju, Y., "In Situ Species Diagnostics and Kinetic Study of Plasma Activated Ethylene Pyrolysis and Oxidation in a Low Temperature Flow Reactor," *Proceedings of the Combustion Institute*, Vol. 35, 2015, pp. 3505–3512.

[26]  Wang, H., You, X., Joshi, A. V., Davis, S. G., Laskin, A., Egolfopoulos, F., and Law, C. K., "USC Mech Version II. High-Temperature Combustion Reaction Model of H2/CO/C1-C4 Compounds," Univ. of Southern California, Los Angeles, CA, 2007, p. 2011, http://ignis.usc.edu/USC_Mech_II.htm.

[27]  Burke, M. P., Chaos, M., Ju, Y., Dryer, F. L., and Klippenstein, S. J., "Comprehensive H2/O2 Kinetic Model for High-Pressure Combustion," *International Journal of Chemical Kinetics*, Vol. 44, No. 7, 2012, pp. 444–474.
doi:10.1002/kin.v44.7

[28]  Shen, X., Yang, X., Santner, J., Sun, J., and Ju, Y., "Experimental and Kinetic Studies of Acetylene Flames at Elevated Pressures," *Proceedings of the Combustion Institute*, Vol. 35, No. 1, 2015, pp. 721–728.

[29]  Lefkowitz, J. K., Guo, P., Rousso, A., and Ju, Y., "Species and Temperature Measurements of Methane Oxidation in a Nanosecond Repetitively Pulsed Discharge," *Philosophical Transactions of the Royal Society of London, Series A: Mathematical and Physical Sciences*, Vol. 373, No. 2048, 2015, pp. 1–21.
doi:10.1098/rsta.2014.0333

[30]  Nagaraja, S., and Yang, V., "A 'Frozen Electric-Field' Approach to Simulate Repetitively Pulsed Nanosecond Plasma Discharges and Ignition of Hydrogen–Air Mixtures," *Journal of Physics D: Applied Physics*, Vol. 47, No. 38, 2014, pp. 1–11.
doi:10.1088/0022-3727/47/38/385201

[31]  Nagaraja, S., Yang, V., and Adamovich, I., "Multi-Scale Modelling of Pulsed Nanosecond Dielectric Barrier Plasma Discharges in Plane-to-Plane Geometry," *Journal of Physics D: Applied Physics*, Vol. 46, No. 15, 2013, pp. 1–13.
doi:10.1088/0022-3727/46/15/155205

[32]  Yang, S., Nagaraja, S., Yang, V., Sun, W., Lefkowitz, J. K., and Ju, Y., "Numerical and Experimental Investigation of Nanosecond-Pulsed Plasma Activated C2H4/O2/Ar Mixtures in a Low Temperature Flow Reactor," *53rd AIAA Aerospace Sciences Meeting*, AIAA Paper 2015-1614, 2015.

[33]  Macheret, S. O., Shneider, M. N., and Miles, R. B., "Modeling of Air Plasma Generation by Repetitive High-Voltage Nanosecond Pulses," *IEEE Transactions on Plasma Science*, Vol. 30, No. 3, 2002, pp. 1301–1314.
doi:10.1109/TPS.2002.802142

[34]  Wang, Q., Economou, D. J., and Donnelly, V. M., "Simulation of a Direct Current Microplasma Discharge in Helium at Atmospheric Pressure," *Journal of Applied Physics*, Vol. 100, No. 2, 2006, Paper 023301.
doi:10.1063/1.2214591

[35]  Incropera, F. D., Bergman, D., and Lavine, T. A., *Fundamentals of Heat and Mass Transfer*, Wiley, New York, 2007, pp. 310–317.

[36]  Yang, S., Kurganov, A., and Liu, Y., "Well-Balanced Central Schemes on Overlapping Cells with Constant Subtraction Techniques for the Saint-Venant Shallow Water System," *Journal of Scientific Computing*, Vol. 63, No. 3, 2015, pp. 678–698.
doi:10.1007/s10915-014-9908-z

[37]  Hagelaar, G., and Pitchford, L., "Solving the Boltzmann Equation to Obtain Electron Transport Coefficients and Rate Coefficients for Fluid Models," *Plasma Sources Science and Technology*, Vol. 14, No. 4, 2005, pp. 722–733.
doi:10.1088/0963-0252/14/4/011

[38]  Hayashi, M., "Hayashi Database," www.lxcat.net/Hayashi [retrieved 31 March 2014].

[39]  Alves, L. L., and Ferreira, C. M., "IST-Lisbon Database," www.lxcat.net/IST-Lisbon [retrieved 31 March 2014].

[40]  Itikawa, Y., "Itikawa Database," www.lxcat.net/Itikawa [retrieved 31 March 2014].

[41]  Morgan, W. L., "Morgan Database," www.lxcat.net/Morgan [retrieved 31 March 2014].

[42]  Janev, R. K., and Reiter, D., "Unified Analytic Representation of Hydrocarbon Impurity Collision Cross-Sections," *Journal of Nuclear Materials*, Vols. 313–316, No. 1, 2003, pp. 1202–1205.
doi:10.1016/S0022-3115(02)01569-6

[43]  Sun, W., Uddi, M., Won, S. H., Ombrello, T., Carter, C., and Ju, Y., "Kinetic Effects of Non-Equilibrium Plasma-Assisted Methane Oxidation on Diffusion Flame Extinction Limits," *Combustion and Flame*, Vol. 159, No. 1, 2012, pp. 221–229.
doi:10.1016/j.combustflame.2011.07.008

[44]  Pancheshnyi, S., Eismann, B., Hagelaar, G., and Pitchford, L. C., "Computer Code ZDPlasKin," Univ. of Toulouse, LAPLACE, CNRS-UPS-INP, Toulouse, France, 2008, http://www.zdplaskin.laplace.univ-tlse.fr.

[45] Capitelli, M., Ferreira, C. M., Gordiets, B. F., and Osipov, A. I., *Plasma Kinetics in Atmospheric Gases*, Springer–Verlag, Berlin, 2000, pp. 158–163.

[46] Kossyi, I. A., Kostinsky, A. Y., Matveyev, A. A., and Silakov, V. P., "Kinetic Scheme of the Non-Equilibrium Discharge in Nitrogen-Oxygen Mixtures," *Plasma Sources Science and Technology*, Vol. 1, No. 3, 1992, pp. 207–220.
doi:10.1088/0963-0252/1/3/011

[47] Fletcher, I. S., and Husain, D., "The Collisional Quenching of Electronically Excited Oxygen Atoms, O (21 D 2), by the gases NH3, H2O2, C2H6, C3H8, and C (CH3) 4, Using Time-Resolved Attenuation of Atomic Resonance Radiation," *Canadian Journal of Chemistry*, Vol. 54, No. 11, 1976, pp. 1765–1770.
doi:10.1139/v76-251

[48] Atkinson, R., Baulch, D., Cox, R., Hampson, R., Jr., Kerr, J., Rossi, M., and Troe, J., "Evaluated Kinetic and Photochemical Data for Atmospheric Chemistry: Supplement VI. IUPAC Subcommittee on Gas Kinetic Data Evaluation for Atmospheric Chemistry," *Journal of Physical and Chemical Reference Data*, Vol. 26, No. 6, 1997, pp. 1329–1499.
doi:10.1063/1.556010

[49] DeMore, W. B., Sander, S. P., Golden, D. M., Hampson, R. F., Kurylo, M. J., Howard, C. J., Ravishankara, A. R., Kolb, C. J., and Molina, M. J., "Chemical Kinetics and Photochemical Data for Use in Stratospheric Modeling: Evaluation No. 11 of the NASA Panel for Data Evaluation", Jet Propulsion Lab., Pasadena, CA, 1994, pp. 1–2.

[50] Kajimoto, O., and Fueno, T., "Relative Rate Constants of O (1 D 2)—Olefin Reactions," *Chemical Physics Letters*, Vol. 64, No. 3, 1979, pp. 445–447.
doi:10.1016/0009-2614(79)80218-3

[51] Miyoshi, A., Yoshida, J.-I., Shiki, N., Koshi, M., and Matsui, H., "Product Branching Fractions for the Reaction of O (3 P) with Ethene," *Physical Chemistry Chemical Physics*, Vol. 11, No. 33, 2009, pp. 7318–7323.
doi:10.1039/b905787k

[52] Matsumi, Y., Tonokura, K., Inagaki, Y., and Kawasaki, M., "Isotopic Branching Ratios and Translational Energy Release of Hydrogen and Deuterium Atoms in Reaction of Oxygen (1D) Atoms with Alkanes and Alkyl Chlorides," *Journal of Physical Chemistry*, Vol. 97, No. 26, 1993, pp. 6816–6821.
doi:10.1021/j100128a012

[53] Tully, J. C., "Reactions of O (1D) with Atmospheric Molecules," *Journal of Chemical Physics*, Vol. 62, No. 5, 1975, pp. 1893–1898.
doi:10.1063/1.430675

[54] Bradley, J. N., Edwards, A. D., and Gilbert, J. R., "The Gas-Phase Reactions of Singlet Oxygen Atoms with Methane," *Journal of the Chemical Society A: Inorganic, Physical, Theoretical*, Vol. 1, No. 1, 1971, pp. 326–331.

[55] Flitti, A., and Pancheshnyi, S., "Gas Heating in Fast Pulsed Discharges in N 2–O 2 Mixtures," *The European Physical Journal — Applied Physics*, Vol. 45, No. 02, 2009, pp. 1–7.
doi:10.1051/epjap/2009011

[56] Popov, N., "Fast Gas Heating in a Nitrogen–Oxygen Discharge Plasma: I. Kinetic Mechanism," *Journal of Physics D: Applied Physics*, Vol. 44, No. 28, 2011, pp. 1–16.
doi:10.1088/0022-3727/44/28/285201

[57] Ray, D. J. M., Diaz, R. R., and Waddington, D. J., "Gas-Phase Oxidation of Butene-2: The Role of Acetaldehyde in the Reaction," *Symposium (International) on Combustion*, Vol. 14, No. 1, 1973, pp. 259–266.

[58] "CHEMKIN-PRO 15131," Reaction Design: San Diego, 2013.

A. K. Gupta
*Associate Editor*